***The following resources related to this article are available online at www.sciencemag.org
(this information is current as of March 23, 2010):***

Updated information and services, including high-resolution figures, can be found in the online version of this article at:
http://www.sciencemag.org/cgi/content/full/327/5970/1246

Supporting Online Material can be found at:
http://www.sciencemag.org/cgi/content/full/327/5970/1246/DC1

A list of selected additional articles on the Science Web sites **related to this article** can be found at:
http://www.sciencemag.org/cgi/content/full/327/5970/1246#related-content

This article **cites 25 articles**, 2 of which can be accessed for free:
http://www.sciencemag.org/cgi/content/full/327/5970/1246#otherarticles

This article has been **cited by** 1 articles hosted by HighWire Press; see:
http://www.sciencemag.org/cgi/content/full/327/5970/1246#otherarticles

This article appears in the following **subject collections**:
Atmospheric Science
http://www.sciencemag.org/cgi/collection/atmos

liquid sample (6–9) lies at least partly in the different H_2SO_4 profiles. Because of nearly uniform H_2SO_4 concentrations in case of in situ experiments (5, 12, 13), particles have much more time to grow to detectable sizes. In the case of a point source, $[H_2SO_4]$ decreases rapidly with time (fig. S3) (17), and the growth is not efficient enough. We have conducted experiments with these two approaches by using the same flow tube and detectors. Therefore, the differences arising from different experimental geometries and different detectors are eliminated in our study.

In conclusion, we have shown that the mystery concerning the apparent disagreement of several orders of magnitude in the nucleation rates and 2 to 3 orders of magnitude in the onset $[H_2SO_4]$ between the in situ–produced H_2SO_4 and the H_2SO_4 from a liquid sample does not exist. Therefore, the role of other sulfur-containing species (13), like HSO_5, seems to be of minor importance in the nucleation process, even though these other pathways cannot be completely excluded. Furthermore, we showed that nucleation occurs at atmospherically relevant H_2SO_4 concentrations. The relation between the nucleation rate and H_2SO_4 concentration $[d(\ln J)/d(\ln[H_2SO_4]) = 1.0$ to $2.1]$ from our experiment is consistent with the corresponding atmosphere observations. A nucleation rate of unity is observed at a $[H_2SO_4]$ slightly above 10^6 molecules cm^{-3}, which is well in line with most atmospheric data (1–4, 28, 29). However, in certain locations co-occurrence of nucleation mechanisms involving other species is plausible. We also showed that H_2SO_4 condensation has a dominating contribution to the observed particle growth in our experiment. The growth rate of $(6 \pm 2) \times 10^{-11}$ $[H_2SO_4]$ cm^3 molecules^{-1} nm s^{-1} obtained from

our data is close to the theoretical estimate of pure H_2SO_4 condensation and is smaller than ambient growth rates, which supports the findings that in the atmosphere, compounds like organics (30, 31) or ammonia (32) are involved in the early growth process. Even though the exact nucleation mechanism remains an open question, our results show that H_2SO_4 at atmospheric concentrations can explain atmospheric nucleation rates in most locations even without clear participation of ammonia or organic substances. Therefore, our findings can be used straightforwardly in further model studies, including climate models.

References and Notes

1. R. J. Weber et al., Chem. Eng. Commun. **151**, 53 (1996).
2. S.-L. Sihto et al., Atmos. Chem. Phys. **6**, 4079 (2006).
3. C. Kuang, P. H. McMurry, A. V. McCormick, F. L. Eisele, J. Geophys. Res. **113**, (D10), D10209 (2008).
4. I. Riipinen et al., Atmos. Chem. Phys. **7**, 1899 (2007).
5. T. Berndt, O. Böge, F. Stratmann, J. Heintzenberg, M. Kulmala, Science **207**, 698 (2005).
6. B. E. Wyslouzil, J. H. Seinfeld, R. C. Flagan, K. Okuyama, J. Phys. Chem. **94**, 6842 (1991).
7. Y. Viisanen, M. Kulmala, A. Laaksonen, J. Chem. Phys. **107**, 920 (1997).
8. S. M. Ball, D. R. Hanson, F. L. Eisele, P. H. McMurry, J. Geophys. Res. **104** (D19), 23709 (1999).
9. R. Zhang et al., Science **304**, 1487 (2004).
10. P. H. McMurry, J. Colloid Interface Sci. **78**, 513 (1980).
11. J. P. Friend, R. A. Barnes, R. M. Vasta, J. Phys. Chem. **84**, 2423 (1980).
12. T. Berndt, O. Böge, F. Stratmann, Geophys. Res. Lett. **33**, L15817 (2006).
13. T. Berndt et al., Atmos. Chem. Phys. **8**, 6365 (2008).
14. L.-H. Young et al., Atmos. Chem. Phys. **8**, 4997 (2008).
15. D. R. Benson, Geophys. Res. Lett. **35**, 11801 (2008).
16. D. Kashchiev, J. Chem. Phys. **76**, 5098 (1982).
17. Materials and methods are available as supporting material on Science Online.
18. F. Eisele, D. Tanner, J. Geophys. Res. **98**, (D5), 9001 (1993).
19. M. Sipilä et al., Aerosol Sci. Technol. **43**, 126 (2009).
20. L. A. Sgro, J. Fernández de la Mora, Aerosol Sci. Technol. **38**, 1 (2004).
21. K. E. J. Lehtinen, M. Kulmala, Atmos. Chem. Phys. **3**, 251 (2003).
22. M. Kulmala et al., J. Aerosol Sci. **35**, 143 (2004).
23. C. D. O'Dowd et al., J. Geophys. Res. **107**, 8108 (2002).
24. K. Iida, M. R. Stolzenburg, P. H. McMurry, J. N. Smith, J. Geophys. Res. **113**, (D5), D05207 (2008).
25. M. Kulmala, K. E. J. Lehtinen, A. Laaksonen, Atmos. Chem. Phys. **6**, 787 (2006).
26. B. K. Ku, J. Fernández de la Mora, Aerosol Sci. Technol. **43**, 241 (2009).
27. M. Kulmala et al., Science **318**, 89 (2007).
28. R. J. Weber et al., Geophys. Res. Lett. **26**, 307 (1999).
29. W. Birmili, A. Wiedensohler, C. Plass-Dülmer, H. Berresheim, Geophys. Res. Lett. **27**, 2205 (2000).
30. J. N. Smith et al., Geophys. Res. Lett. **35**, L04808 (2008).
31. C. D. O'Dowd, P. Aalto, K. Hämeri, M. Kulmala, T. Hoffmann, Nature **416**, 497 (2002).
32. J. N. Smith et al., J. Geophys. Res. **110**, (D22), D22S03 (2005).
33. We thank K. Pielok and A. Rohmer for technical assistance and J. Heitzenberg, K.E.J. Lehtinen, V.-M. Kerminen, and M. McGrath for help preparing the manuscript. C. D. O'Dowd is acknowledged for providing the PHA-UCPC instrument. K. Lehtipalo is acknowledged for assistance with the PHA-UCPC, J. Mikkilä and E. Siivola for constructing the PSM, R. Taipale for help with the PTR-MS, J. Hakala and K. Neitola for assistance with experiments, and T. Nieminen for useful discussions. This work was partially funded by European Commision 6th Framework program project European Integrated Project on Aerosol, Cloud, Climate, and Air Quality Interactions (EUCAARI), contract 036833-2. Financial support from Kone foundation, Väisälä foundation, Otto Malm foundation, the Academy of Finland and European Research Council is acknowledged.

Extensive Methane Venting to the Atmosphere from Sediments of the East Siberian Arctic Shelf

Natalia Shakhova,[1,2]*† Igor Semiletov,[1,2]* Anatoly Salyuk,[2] Vladimir Yusupov,[2] Denis Kosmach,[2] Örjan Gustafsson[3]

Remobilization to the atmosphere of only a small fraction of the methane held in East Siberian Arctic Shelf (ESAS) sediments could trigger abrupt climate warming, yet it is believed that sub-sea permafrost acts as a lid to keep this shallow methane reservoir in place. Here, we show that more than 5000 at-sea observations of dissolved methane demonstrates that greater than 80% of ESAS bottom waters and greater than 50% of surface waters are supersaturated with methane regarding to the atmosphere. The current atmospheric venting flux, which is composed of a diffusive component and a gradual ebullition component, is on par with previous estimates of methane venting from the entire World Ocean. Leakage of methane through shallow ESAS waters needs to be considered in interactions between the biogeosphere and a warming Arctic climate.

The terrestrial and continental shelf regions of the Arctic contain a megapool of carbon in shallow reservoirs (1–3), most of which is presently sequestered in permafrost (4, 5). Sustained release of methane (CH_4) to the atmosphere from thawing Arctic permafrost is a likely positive feedback to climate warming (5, 6). Arctic CH_4 releases are implied in both past climate shifts (7, 8) and the renewed growth of contemporary atmospheric CH_4 (9, 10). Observed Arctic warming in early 21st century is stronger than predicted by several degrees (fig. S1A) (11–14), which may accelerate the thaw-release of CH_4 in a positive feedback. Investigations of Arctic CH_4 releases have focused on thawing permafrost structures on land (2, 4–6, 15, 16) with a scarcity of observations of CH_4 in the extensive but inaccessible East Siberian Arctic Seas (ESAS), where warming is particularly pronounced (fig. S1A) (11).

The ESAS (encompassing the Laptev, East Siberian, and Russian part of the Chuckchi seas) occupies an area of 2.1×10^6 km^2, three times as great as that of terrestrial Siberian wetlands. It is a shallow seaward extension of the Siberian tundra that was flooded during the Holocene transgression 7 to 15 thousand years ago (17, 18). The ESAS sub-sea permafrost (fig. S1B), which is frozen sediments interlayered with the flooded peatland (18), not only contains comparable amounts of carbon as still land-fast permafrost in the Siberian tundra but also hosts permafrost-related seabed deposits of CH_4 (19). Moreover, ESAS sub-sea

permafrost is potentially more vulnerable to thawing than terrestrial permafrost. In contrast to on-land permafrost, sub-sea permafrost has experienced a drastic change in its thermal regime because of the seawater inundation. The annual average temperature of ESAS bottom seawater ($-1.8°$ to $1°C$) is $12°$ to $17°C$ warmer than the annual average surface temperature over on-land permafrost (18, 19). A physical implication of combined bottom-up geothermal and top-down seawater heat fluxes is the partial thawing and failure of sub-sea permafrost and thus an increased permeability for gases. We consequently hypothesized that CH_4 is released from seabed deposits to vent extensively to the Arctic atmosphere.

To test our hypothesis, we have undertaken annual field campaigns (August to September, 2003 to 2008; six cruises in total), one helicopter survey (September 2006), and one over-ice winter expedition (April 2007) (20, 21). On the basis of a more limited coverage, we previously demonstrated that CH_4 is released from ESAS sediments to the overlying water column (22, 23). The objective of the present study is an integrated assessment of multiple years of observations for

[1]International Arctic Research Centre, University of Alaska, Fairbanks, AK 99709, USA. [2]Russian Academy of Sciences, Far Eastern Branch, Pacific Oceanological Institute, Vladivostok 690041, Russia. [3]Stockholm University, Bert Bolin Centre for Climate Research and Department of Applied Environmental Science, Stockholm S-10691, Sweden.

*These authors contributed equally to this work.
†To whom correspondence should be addressed. E-mail: nshakhov@iarc.uaf.edu

the whole of the ESAS in order to provide an estimate of the venting flux of CH_4 to the atmosphere over the entire ESAS. It is this estimate of CH_4 flux to the atmosphere that has been missing and has prohibited a quantitative evaluation of the putative climate impact of ESAS CH_4. The CH_4 flux estimates are based on 5100 seawater samples from 1080 stations—a larger database than for any previous ocean CH_4 study (24)—geographically distributed over the ESAS (Fig. 1A). The "landscape" of coastal waters is fortunately less heterogeneous than the terrestrial tundra counterpart. Hence, this assessment of coastal CH_4 fluxes may be contrasted with up-scaling challenges facing estimates of greenhouse gas emissions from the tundra, which nonetheless are usually limited to measurements at a few sites (4–6, 15, 16).

The dissolved CH_4 concentrations in ESAS during summers of 2003 to 2008 demonstrate a ubiquitous supersaturation over large spatial scales. Although there are some spatial and vertical gradients, the emerging picture is that most of the ESAS is supersaturated with CH_4 in the near-bottom waters (Fig. 1B), with >50% of the ESAS surface waters being supersaturated (Fig. 1C). The median summertime supersaturation was 880% in background areas and 8300% in hotspot areas [supporting online material (SOM) text] (21). Besides the vertical profiles with maximums near the seafloor, which is common to the oceanic water column (25), the dissolved CH_4 distribution in the ESAS varied to maximum near the surface and had uniform distribution throughout the water column.
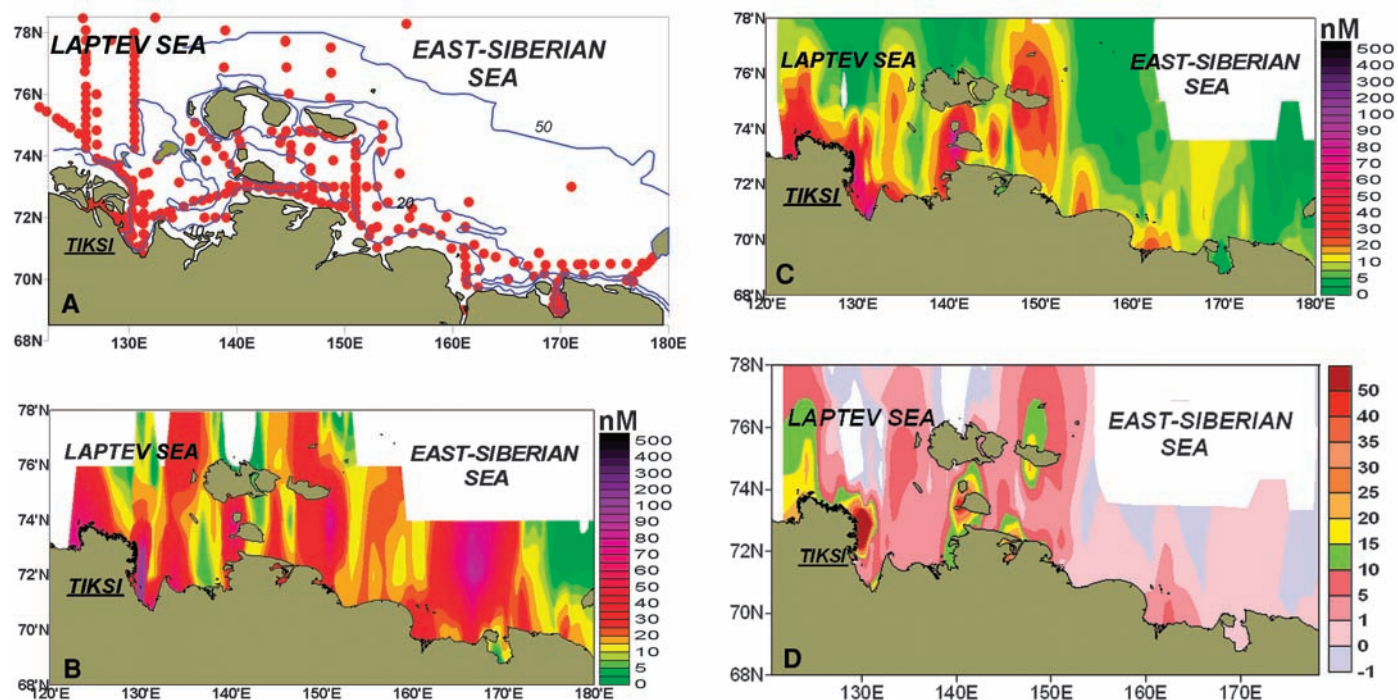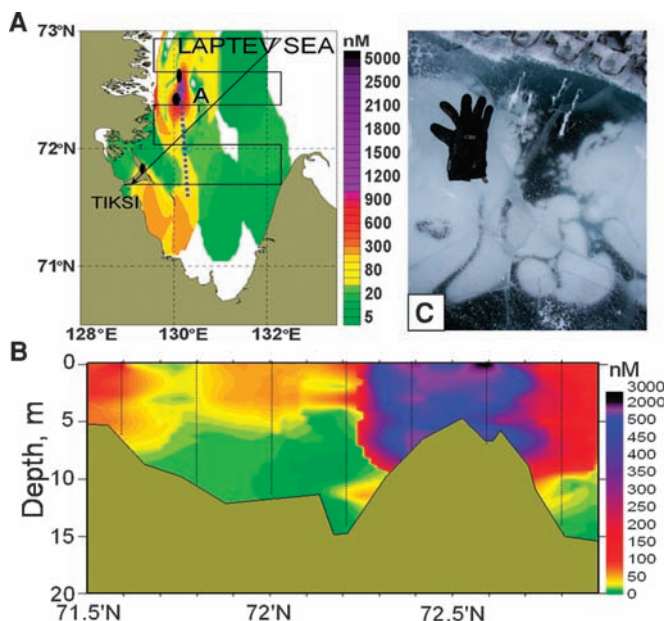
Both the bottom- and surface-water–dissolved CH_4 concentrations in winter (~$5°$ to $7°C$ colder than in summer), which were measured in the studied area beneath the sea ice (Fig. 2A), were 5 to 10 times higher than in summer yet had the same distribution within the water column (Fig. 2B). Such vertical profiles point to a rapid transport mechanism such as ebullition, which is considered to be a predominant mechanism of CH_4 transport in shallow waters and particularly when CH_4 releases from seabed deposits (26). Large bubbles of gas entrapped within the fast (annual) sea ice were observed in winter (Fig. 2C), with CH_4 concentrations of up to 11,400 parts per million by volume (ppmv). Manifestations of ebullition were furthermore registered acoustically as bubble clouds, which rose from the seabed throughout the entire water column or, at deeper locations, to subsurface layers (fig. S2). Taken together, the observations demonstrate that the ESAS—the world's largest continental shelf sea—is perennially laden with CH_4 all the way up to the sea surface.

The horizontal and vertical CH_4 distributions indicate a sedimentary source, yet other sources were considered. Riverborne export of CH_4 was excluded on the basis of measurements in, for example, the Bykovskaya Channel, which is the main outflow of the Lena River (fig. S3). Dissolved CH_4 concentrations decreased downstream through the delta channel and then increased again in coastal waters, suggesting separate sources. Production of CH_4 in the water column was also deemed unlikely to account for the high ESAS concentrations. Mixed-layer maxima of CH_4 in

Fig. 1. Summertime observations of dissolved CH_4 in the ESAS (21). (**A**) Positions of oceanographic stations in the eastern Laptev Sea and East Siberian Sea; bathymetry lines for 10, 20, and 50 m depth are shown in blue. (**B**) Dissolved CH_4 in bottom water. (**C**) Dissolved CH_4 in surface water. (**D**) Fluxes of CH_4 venting to the atmosphere over the ESAS.

the open ocean in the 4-to 10-nM range have been suggested to be associated with either high rates of primary production, methanogenesis inside anaerobic microenvironments of sinking particles (25, 27), or through decomposition of methylphosponates in the tropical ocean (28). ESAS primary production is suppressed by factors of 100 to 1000 as compared with that of the open ocean because of lack of sunlight and highly turbid waters, whereas CH_4 levels are 10-fold larger (Fig. 1, B and C). The acoustic-geophysical record combined with the vertical CH_4 profiles suggest that the water column inventory in the ESAS stems from sedimentary release. Because the ESAS average depth is only 45 m, the water column provides a short conduit for bottom-released CH_4 to be vented to the overlying atmosphere (Fig. 1D). This distinguishes CH_4 venting in the ESAS from sedimentary releases in deeper waters, in which the bulk of CH_4 would be oxidized before reaching the sea surface (25, 29).

Mixing ratios of CH_4 in the atmospheric boundary layer provide direct evidence for CH_4 escape. For instance, high-frequency surveying along the >4000-km Northeast Passage demonstrates a consistently elevated mixing ratio of CH_4, relative to the latitude-specific monthly mean (LSMM) (30), and with extreme variability (Fig. 3A), as is expected near sources. From values averaging 2.10 ± 0.02 parts per million (ppm) (1 SD) through the Kara Sea, the CH_4 mixing ratio increased markedly after passage through the Vilkitskyi Strait and entering the ESAS, averaging 2.97 ± 0.15 ppm in the Laptev Sea and 2.66 ± 0.09 ppm in the East Siberian Sea, with spikes in the 6.4 to 8.2 ppm range. A helicopter-mounted survey over the Laptev Sea during September 2006 demonstrated that the CH_4 mixing ratio in the atmosphere was elevated by 5 to 10% up to 1800 m in height (Fig. 3B).

To estimate the total annual CH_4 flux (F_t) from the ESAS, six separate components of the total flux budget were considered to account for differences in ice coverage [summer (F_{ts}) versus winter (F_{tw})] and mechanism of water column transfer [diffusive-dissolved (F_{td}) versus ebullition-bubbles (F_{te})] integrated over the areal extent of the two regions with different source strengths [background (F_{tb}) versus hotspots (F_{th})] (31).

Mean diffusive fluxes were estimated by means of the surface-film model for each population (32). The summertime ebullition component was taken as the difference between the total flux as measured directly with eddy covariance techniques (33–35), and this calculated the diffusive flux. Hence, the averaged CH_4 flux, based on mean daily actual wind speed for the 90 percentile of the data set, yielded a mean flux of 3.67 mg m^{-2} d^{-1}, which was prorated to the background area of 1.9×10^6 km^2. A mean flux of 11.8 mg m^{-2} d^{-1} was prorated to the area of the hotspots (0.2×10^6 km^2). Summertime diffusive contribution of the background area was thus composed of 0.69 Tg C-CH_4, and hotspots added 0.24 Tg C-CH_4 to the total summertime diffusive flux of 0.93 Tg C-CH_4 ($F_{ds} = F_{dsb} + F_{dsh}$) (Table 1). The total summer flux in background areas (F_{tsb}) was 1.56 Tg C-CH_4, which thus constrains the ebullition component (F_{esb}) to 0.87 Tg C-CH_4 ($F_{tsb} = F_{dsb} + F_{esb}$). The total summertime CH_4 flux in hotspot areas (F_{tsh}) was 0.63 Tg C-CH_4, with 0.39 Tg C-CH_4 as the ebullition component (F_{seh}) ($F_{tsh} = F_{dsh} + F_{seh}$). Total CH_4 flux for the period of open water thus reaches 2.19 Tg C-CH_4 ($F_{ts} = F_{tsb} + F_{tsh}$).

For the winter period, dissolved CH_4 concentrations beneath the sea ice were 5 to 10 times higher than in the summer (Figs. 1 and 2). Hence, we assume that CH_4 concentrations, accumulating beneath the sea ice, represent the sum of the diffusive (potentially accumulated) winter flux component (F_{dw}) and ebullition winter flux component (F_{ew}; potentially accumulated as increased CH_4 from dissolution of most bubbles during storage under the ice) (Table 1). Given a constant rate of CH_4 release from the seabed throughout the year, the 265-days-long ice-covered period in

Fig. 2. Wintertime observations of dissolved CH_4 in the ESAS (21). (**A**) Dissolved CH_4 measured beneath the sea ice. (**B**) Vertical distribution of dissolved CH_4 along the transect, shown as a blue dotted line in (A). (**C**) Bubbles of gas entrapped within the sea ice were ubiquitously observed [the diameter of the borehole is ~37 cm (72.59°N, 130.11°E), April 2007]. The black-arrow raster line shows the route of the helicopter-based air CH_4 survey in September 2006.
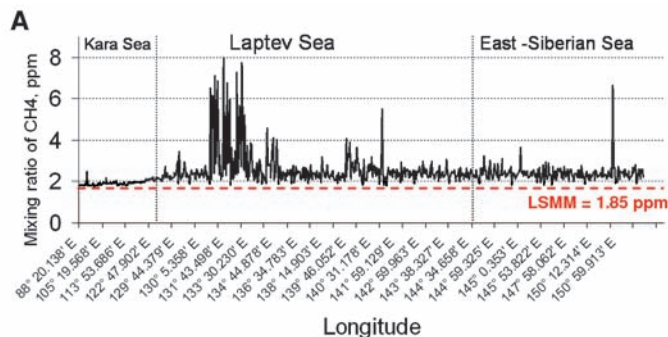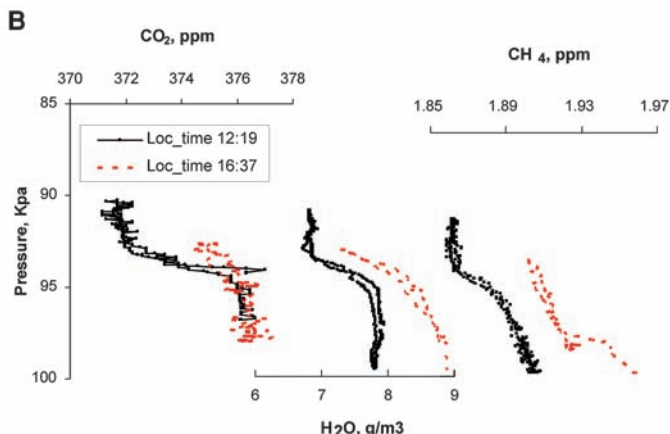

Fig. 3. Survey of CH_4 mixing ratio in the atmospheric boundary layer along the northern Eurasian seaboard (21). (**A**) Mixing ratio of CH_4 in the air above the water surface measured along the ship route in September 2005 (red dotted line shows the LSSM of 1.85 ppmv established for the Barrow, Alaska, USA, monitoring station at 71° 19' N, 156° 35' W (www.cmdl.noaa.gov/ccgg/insitu.html). The position of the transects are shown as color dotted lines in fig. S1B. Red, the Kara Sea; black, the Laptev Sea; orange, the East Siberian Sea. (**B**) Vertical mixing ratio of CH_4 in the atmosphere above southeast Laptev Sea (72.49°N, 130.51°E) as measured during a helicopter survey in September 2006 (the helicopter route is shown as black-arrows in Fig. 2A).

Table 1. Components of the annual CH_4 flux in the ESAS. In a_c^b, a is the mean, b is the 95% upper confidence limit of the flux, and c is the 95% lower confidence limit of flux. F_{dsb}, diffusive summer flux in background areas; F_{dsh}, diffusive summer flux in hotspots; F_{ds}, total diffusive summer flux ($F_{ds} = F_{dsb} + F_{dsh}$); F_{esb}, ebullition summer flux component in background areas; F_{esh}, ebullition summer flux component in hotspots; F_{es}, total ebullition summer flux component ($F_{es} = F_{esb} + F_{esh}$); F_{dwb}, diffusive winter flux in background areas; F_{dwh}, diffusive winter flux in hotspots; F_{dw}, total diffusive winter flux ($F_{dw} = F_{dwb} + F_{dwh}$); F_{ewb}, ebullition winter flux component in background areas; F_{ewh}, ebullition winter flux component in hotspots; F_{ew}, total ebullition winter flux component ($F_{ew} = F_{ewb} + F_{ewh}$); F_{tsb}, total summer flux in background areas ($F_{tsb} = F_{dsb} + F_{esb}$); F_{tsh}, total summer flux in hotspots ($F_{tsh} = F_{dsh} + F_{esh}$); F_{ts}, total summer flux ($F_{ts} = F_{tsb} + F_{tsh}$); F_{twb}, total winter flux in background areas ($F_{twb} = F_{dwb} + F_{ewb}$); F_{twh}, total winter flux in hotspots ($F_{twh} = F_{dwh} + F_{ewh}$); F_{tw}, total winter flux ($F_{tw} = F_{twb} + F_{twh}$); F_{tb}, total flux in background areas ($F_{tb} = F_{tsb} + F_{twb}$); F_{th}, total flux in hotspots ($F_{th} = F_{tsh} + F_{twh}$); F_t, total annual flux ($F_t = F_{tb} + F_{th}$). The methods to calculate the fluxes and to derive the statistical population parameters for each flux component are presented in (21) and the SOM text, and the parameters used for calculations are described in table S2.

Component name	Background	Hotspots	Total
Area (km^2)	1.9×10^6	0.2×10^6	2.1×10^6
Diffusive summer flux (Tg $C-CH_4$), F_{dsb}, F_{dsh}, F_{ds}	$0.69_{0.51}^{0.71}$	$0.24_{0.17}^{0.31}$	$0.93_{0.68}^{1.01}$
Ebullition summer flux (Tg $C-CH_4$), F_{esb}, F_{esh}, F_{es}	$0.87_{0.65}^{1.26}$	$0.39_{0.38}^{0.41}$	$1.26_{1.03}^{1.67}$
Total summer CH_4 flux (Tg $C-CH_4$), F_{tsb}, F_{tsh}, F_{ts}	$1.56_{1.17}^{1.97}$	$0.63_{0.55}^{0.71}$	$2.19_{1.71}^{2.68}$
Diffusive winter (accumulative potential) flux (Tg $C-CH_4$), F_{dwb}, F_{dwh}, F_{dw}	$1.8_{1.32}^{1.84}$	$0.62_{0.44}^{0.78}$	$2.42_{1.76}^{2.62}$
Ebullition winter flux, (Tg $C-CH_4$), F_{ewb}, F_{ewh}, F_{ew}	$2.2_{1.69}^{3.2}$	$1.17_{1.14}^{1.23}$	$3.37_{2.83}^{4.43}$
Total winter (accumulative potential) flux (Tg $C-CH_4$), F_{wb}, F_{wh}, F_w	$4.0_{3.01}^{5.04}$	$1.79_{1.58}^{2.01}$	$5.79_{4.59}^{7.05}$
Total annual flux (Tg $C-CH_4$), F_{tb}, F_{th}, F_t	$5.56_{4.18}^{7.01}$	$2.42_{2.13}^{2.72}$	$7.98_{6.31}^{9.73}$

the ESAS (F_{dwb}) could thus accumulate 1.8 Tg of $C-CH_4$ from the background areas and an additional 0.62 Tg $C-CH_4$ from the hotspots (F_{dwh}) to yield a total diffusive wintertime flux of 2.42 Tg of $C-CH_4$ ($F_{dw} = F_{dwb} + F_{dwh}$), with a portion vented to the atmosphere through wintertime polynyas and the rest at ice break-up. Because the ice-covered period is only 2.5 times longer than the ice-free period, whereas concentrations of dissolved CH_4 are 5 to 10 times higher, we suggest that contribution of ebullition to annual CH_4 emissions from the ESAS could be significant.

The ebullition component of the flux for the ice-covered period was estimated by applying scaling coefficients according to the relative size of diffusive and ebullition components in the summer. Wintertime ebullition fluxes were thus 2.2 Tg $C-CH_4$ (F_{ewb}) and 1.17 Tg $C-CH_4$ (F_{ewh}), which gives 4.0 Tg $C-CH_4$ in total for the background areas ($F_{twb} = F_{dwb} + F_{ewb}$) and 1.79 Tg $C-CH_4$ for the hotspot areas ($F_{twh} = F_{dwh} + F_{ewh}$). Together with the total summer flux of 2.19 Tg $C-CH_4$, this corresponds to a total annual venting flux of CH_4 to the ESAS atmosphere of $7.98_{6.31}^{9.73}$ Tg $C-CH_4$ (Table 1), which does not include nongradual ebullition. Although such releases of strong CH_4 pulses occur (Fig. 3A and fig. S2, the "spikes"), this component is not included in the total flux estimate, which thus is conservative because the spatial and temporal pattern of such nongradual "catastrophic event" ebullition is uncertain.

The diffusive flux component was about 40% of the total annual CH_4 flux, with the remainder being vented through gradual ebullition (Table 1). The winter component (including ice break-up) was 2.5 times larger than the summer flux and about one third of the total flux emanated from the hotspot areas covering ~10% of the ESAS area. The annual outgassing from the shallow ESAS of $7.98_{6.31}^{9.73}$ Tg $C-CH_4$ is of the same magnitude as existing estimates of total CH_4 emissions from the entire world ocean (1, 25). Although the oceanic CH_4 flux should be revised, the current estimate is not alarmingly altering the contemporary global CH_4 budget. These findings do change our view of the vulnerability of the large sub-sea permafrost carbon reservoir on the ESAS; the permafrost "lid" is clearly perforated, and sedimentary CH_4 is escaping to the atmosphere.

There remains substantial uncertainty regarding several aspects of the CH_4 release from the ESAS. To make predictions of future development of these CH_4 releases, there needs to be progress in the comprehension of the forms and locations of the sedimentary CH_4 sources as well as how each may respond to Arctic change. Multidimensional isotopic analysis of the released CH_4 is one method to apportion the CH_4 sources and to constrain the flux attenuation that is attributable to microbial CH_4 oxidation. The relative importance of the various flux components may also be independently approached by means of detailed observations of atmospheric mixing ratios throughout the year because enhanced venting may be expected during fall breakdown of water column stratification (September to October) and ice breakup (May to July). To discern whether this extensive CH_4 venting over the ESAS is a steadily ongoing phenomenon or signals the start of a more massive CH_4 release period, there is an urgent need for expanded multifaceted investigations into these inaccessible but climate-sensitive shelf seas north of Siberia.

References and Notes

1. Intergovernmental Panel on Climate Change (IPCC), *The Scientific Basis* (Cambridge Univ. Press, New York, 2007).
2. C. Tarnocai et al., *Global Biogeochem. Cycles* **23**, GB2023 (2009).
3. I. S. Gramberg, Yu. N. Kulakov, Yu. E. Pogrebitsky, D. S. Sorokov, *Proc. World Pet. Congr.* **11**, 93 (1983).
4. S. A. Zimov, E. A. G. Schuur, F. S. Chapin III, *Science* **312**, 1612 (2006).
5. E. A. G. Schuur et al., *Nature* **459**, 556 (2009).
6. K. M. Walter, S. A. Zimov, J. P. Chanton, D. Verbyla, F. S. Chapin III, *Nature* **443**, 71 (2006).
7. E. G. Nisbet, J. Chappellaz, *Science* **324**, 477 (2009).
8. V. V. Petrenko et al., *Science* **24**, 506 (2009).
9. W. C. Oechel et al., *Nature* **361**, 520 (1993).
10. M. Rigby et al., *Geophys. Res. Lett.* **35**, L22805 (2008).
11. www.eoearth.org/article/State_of_the_Arctic_Report
12. F. W. Zwiers, *Nature* **416**, 690 (2002).
13. V. M. Kattsov et al., *Arctic Climate Impact Assessment (ACIA) Scientific Report 2004, chap. 4, Future Climate Change: Modeling and Scenarios* (Cambridge Univ. Press, New York, 2005), pp. 99–150.
14. R. W. Lindsay, J. Zhang, A. J. Schweiger, M. A. Steele, H. Stern, *J. Clim.* **22**, 165 (2009).
15. I. P. Semiletov, *J. Atmos. Sci.* **56**, 286 (1999).
16. M. Mastepanov et al., *Nature* **456**, 628 (2008).
17. V. A. Soloviev, Sixth International Conference on Gas in Marine Sediments, St. Petersburg, Russia, 5 to 9 September 2000, abstr. pp. 123–125.
18. N. N. Romanovskii, H.-W. Hubberten, A. V. Gavrilov, A. A. Eliseeva, G. S. Tipenko, *Geo-Mar. Lett.* **25**, 167 (2005).
19. V. A. Soloviev, G. D. Ginzburg, E. V. Telepnev, Yu. N. Mikhaluk, *Cryothermia of Gas Hydrates in the Arctic Ocean* (VNIIOkeangeologia, St. Petersburg, 1987).
20. We deployed our field laboratories on ice-strengthened small- and mid-sized ships that were suitable for operation in shallow ESAS waters. Seawater samples were immediately drawn from conductivity-temperature-depth (CTD)–Niskin bottles and analyzed onboard with gas chromatography (21).

21. Materials and methods are available as supporting material on *Science* Online.
22. N. Shakhova, I. Semiletov, G. Panteleev, *Geophys. Res. Lett.* **32**, L09601 (2005).
23. N. Shakhova, I. Semiletov, *J. Mar. Syst.* **66**, 227 (2007).
24. All the seawater-dissolved CH_4 concentration data are publicly and freely available at http://research.iarc.uaf.edu/SSSS/. A description of this large database as compared with previous ocean CH_4 studies is presented in table S3.
25. W. S. Reeburgh, *Chem. Rev.* **107**, 486 (2007).
26. I. Leifer, B. Luyendyk, J. Boles, J. Clark, *Global Biogeochem. Cycles* **20**, GB3008 (2006).
27. N. J. P. Owens, C. S. Law, R. F. C. Mantoura, P. H. Burkill, C. A. Llewellyn, *Nature* **354**, 293 (1991).
28. D. M. Karl et al., *Nat. Geosci.* **1**, 473 (2008).
29. G. K. Westbrook et al., *Geophys. Res. Lett.* **36**, L15608 (2009).
30. LSMM closest to the study area is established for the Barrow, Alaska, USA, monitoring station at 71° 19′ N,

156° 35′ W (www.cmdl.noaa.gov/ccgg/insitu.html); it is equal to 1.85 ppmv.
31. The division into two subpopulations for background and hotspot areas within the ESAS was based on a statistical approach detailed in SOM text S2.1 and displayed graphically in fig. S4. These two resolved populations were then first subjected to an empirical distribution function (EDF) test (SOM text S1.1). The results of the EDF test (table S1) yielded that a lognormal distribution function best fit the data. This function was hence used when applying the maximum likelihood (ML) method to calculate the statistical population parameters mean and variance [expressed as upper and lower 95% confidence limits (equations are provided in SOM text S1.1)]. The derived population parameters, displayed in table S2, were then used to estimate the overall ESAS CH_4 fluxes as summarized in Table 1.
32. R. Wanninkhof, *J. Geophys. Res.* **97** (C5), 7373 (1992).
33. D. D. Baldocchi, *Glob. Change Biol.* **9**, 479 (2003).
34. J. B. Edson, A. A. Hinton, K. E. Prada, J. E. Hare, C. W. Fairall, *J. Atmos. Ocean. Technol.* **15**, 547 (1998).
35. T. Fujitani, *Pap. Meteorol. Geophys.* **36**, 157 (1985).
36. We thank V. Sergienko, G. Golitsyn, S. Akasofu, L. Hinzman, and V. Akulichev for their support of our work in the Siberian Arctic. This research was supported by the International Arctic Research Centre through a National Oceanic and Atmospheric Administration Cooperative Agreement, the Far Eastern Branch of the Russian Academy of Sciences, the Russian Foundation for Basic Research, NSF, the Swedish Research Council, and the Knut and Alice Wallenberg Foundation.

Hippocampal Short- and Long-Term Plasticity Are Not Modulated by Astrocyte Ca²⁺ Signaling

Cendra Agulhon,[1]* Todd A. Fiacco,[2] Ken D. McCarthy[1]

The concept that astrocytes release neuroactive molecules (gliotransmitters) to affect synaptic transmission has been a paradigm shift in neuroscience research over the past decade. This concept suggests that astrocytes, together with pre- and postsynaptic neuronal elements, make up a functional synapse. Astrocyte release of gliotransmitters (for example, glutamate and adenosine triphosphate) is generally accepted to be a Ca^{2+}-dependent process. We used two mouse lines to either selectively increase or obliterate astrocytic G_q G protein–coupled receptor Ca^{2+} signaling to further test the hypothesis that astrocytes release gliotransmitters in a Ca^{2+}-dependent manner to affect synaptic transmission. Neither increasing nor obliterating astrocytic Ca^{2+} fluxes affects spontaneous and evoked excitatory synaptic transmission or synaptic plasticity. Our findings suggest that, at least in the hippocampus, the mechanisms of gliotransmission need to be reconsidered.

Calcium transients in astrocytes are physiologically driven by metabotropic G_q G protein–coupled receptors (G_q GPCRs), which can be activated after neurotransmitter release from presynaptic terminals (1, 2). At Schaffer collateral-CA1 (SC-CA1) synapses in acute hippocampal slices, astrocytes can modulate neuronal activity by elevations in Ca^{2+} that are evoked by the following: (i) uncaging IP_3 or Ca^{2+} in individual astrocytes, (ii) repetitive depolarization of the astrocyte membrane, (iii) mechanical stimulation of an astrocyte, or (iv) bath application of endogenous G_q GPCR agonists. With these pharmacological approaches, astrocyte Ca^{2+} elevations have been reported to trigger gliotransmitter release from astrocytes, resulting in the modulation of synaptic transmission and plasticity through the

activation of presynaptic [for example, group I metabotropic glutamate receptors (mGluRs) or adenosine A(1) receptors (A_1Rs)] or postsynaptic receptors [N-methyl-D-aspartate receptors (NMDARs)] (3–11). To circumvent a number of caveats associated with the pharmacological approaches described above (12–15), we have recently developed and characterized two genetically modified mice [the MrgA1+ and IP₃R2 knockout (KO) mice] that enable either selective activation or inactivation of G_q GPCR Ca^{2+} signaling in astrocytes (13, 16, 17). Within the hippocampus, the stimulation of transgenic MrgA1 G_q GPCRs leads to astrocyte-specific Ca^{2+} responses that mimic the "Ca^{2+} fingerprint" response that is elicited by endogenous G_q GPCRs (13). In hippocampal slices derived from IP₃R2 KO mice (17), G_q GPCR Ca^{2+} signaling is obliterated selectively in 100% of astrocytes without affecting neuronal Ca^{2+} responses (16).

We first tested the possibility that astrocytic G_q GPCR Ca^{2+} is involved in the modulation of spontaneous excitatory postsynaptic currents (sEPSCs). In these and the following experiments,

a high percentage of astrocytes (~90 to 100%) were stimulated so that each CA1 neuron has the vast majority of its synapses embedded in astrocyte processes that elevate Ca^{2+} upon G_q GPCR agonist application. Control experiments showed that MrgA1R expression by itself in astrocytes does not affect basal neuronal activity in a nonspecific manner [supporting online material (SOM) text S1]. MrgA1R agonist Phe-Met-Arg-Phe-NH₂ amide (FMRF, 15 μM) was applied to trigger Ca^{2+} elevations in ~90% of mature MrgA1+ passive astrocytes (13) in cell bodies as well as fine processes (Fig. 1, A and B, boxes/traces 1 to 5, SOM text S2, and movie S1). No significant effect of astrocyte Ca^{2+} elevations on sEPSC frequency and amplitude in CA1 neurons from MrgA1+ mice was found (Fig. 1C and SOM text S3, $n = 7$, $P > 0.05$). To test the possibility that this lack of effect might be caused by the stimulation of a transgenic G_q GPCR, we also stimulated endogenous astrocytic endothelin G_q GPCRs (ETRs), which were selected as optimal candidates because they evoke gliotransmitter release in vitro (18), they are thought to be very weakly expressed by neurons and heavily expressed by brain astrocytes at postnatal day 1 to 30 (19), and no direct effects on neuronal activity have been reported when stimulating ETRs (13). Astrocytic ETR-mediated Ca^{2+} increases in ~100% of astrocytes from wild-type (WT) hippocampal slices [endothelin 1 (ET1) and ET3, 10 nM each; SOM text S4, and fig. S1] had no effect on the frequency or amplitude of sEPSCs (Fig. 1, D to F, and SOM text S5, $n = 5$, $P > 0.05$).

Previous studies using conventional pharmacological approaches have suggested that postsynaptic NMDARs might be preferential targets for glutamate release from astrocytes (3–7, 9, 10), prompting us to examine the possibility that astrocytic G_q GPCR Ca^{2+} elevations modulate the NMDAR-mediated component of evoked whole-cell EPSCs (eEPSCs). FMRF does not produce a nonspecific effect on NMDA eEPSCs (Fig. 2, A and A1, and SOM text S6). FMRF or ETs were

[1]Department of Pharmacology, University of North Carolina at Chapel Hill, Genetic Medicine Building, CB 7365, Chapel Hill, NC 27599, USA. [2]Department of Cell Biology and Neuroscience, University of California Riverside, Riverside, CA 92521, USA.

*To whom correspondence should be addressed. E-mail: cendra_agulhon@med.unc.edu